LANGMUIR

pubs.acs.org/Langmuir Article

Precise Definition of a "Monolayer Point" in Polymer Brush Films for Fabricating Highly Coherent TiO_2 Thin Films by Vapor-Phase Infiltration

Ross Lundy,*,⊥ Pravind Yadav,⊥ Nadezda Prochukhan, Elsa C. Giraud, Tom F. O'Mahony, Andrew Selkirk, Eleanor Mullen, Jim Conway, Miles Turner, Stephen Daniels, P. G. Mani-Gonzalez, Matthew Snelgrove, Justin Bogan, Caitlin McFeely, Robert O'Connor, Enda McGlynn, Greg Hughes, Cian Cummins, and Michael A. Morris*

Cite This: *Langmuir* 2020, 36, 12394−12402 Read Online

ACCESS | Metrics & More | Article Recommendations | Supporting Information

ABSTRACT: In this work, we show that in order to fabricate coherent titania (TiO_2) films with precise thickness control, it is critical to generate a complete polymer brush monolayer. To date, demonstrations of such dense polymer monolayer formation that can be utilized for inorganic infiltration have been elusive. We describe a versatile bottom-up approach to covalently and rapidly (60 s processing) graft hydroxyl-terminated poly(2-vinyl pyridine) (P2VP-OH) polymers on silicon substrates. P2VP-OH monolayer films of varying thicknesses can subsequently be used to fabricate high-quality TiO_2 films. Our innovative strategy is based upon room-temperature titanium vapor-phase infiltration of the grafted P2VP-OH polymer brushes that can produce TiO_2 nanofilms of 2−4 nm thicknesses. Crucial parameters are explored, including molecular weight and solution concentration for grafting dense P2VP-OH monolayers from the liquid phase with high coverage and uniformity across wafer-scale areas (>2 cm^2). Additionally, we compare the P2VP-OH polymer systems with another reactive polymer, poly(methyl methacrylate)-OH, and a relatively nonreactive polymer, poly(styrene)-OH. Furthermore, we prove the latter to be effective for surface blocking and deactivation. We show a simple process to graft monolayers for polymers that are weakly interacting with one another but more challenging for reactive systems. Our methodology provides new insight into the rapid grafting of polymer brushes and their ability to form TiO_2 films. We believe that the results described herein are important for further expanding the use of reactive and unreactive polymers for fields including area-selective deposition, solar cell absorber layers, and antimicrobial surface coatings.

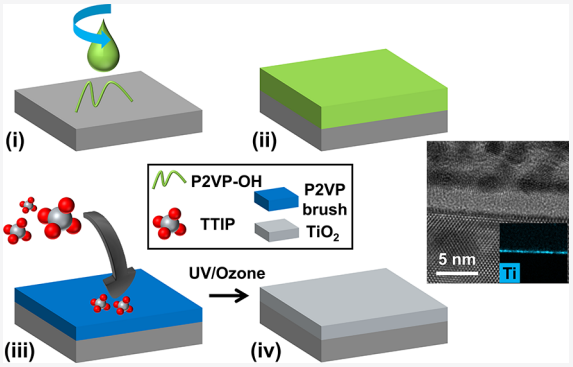

INTRODUCTION

Continued miniaturization of semiconductor devices has led to cost and integration issues[1] which challenge the manufacture of a 3 nm node as envisaged by semiconductor foundries for 2023.[2,3] Gate voltage scaling at these dimensions necessitates state-of-the-art architectures beyond fin field-effect transistors (FETs) such as the gate-all-around FET technology, leading to further integration complexity.[4] Approaches complimenting photolithography include nanoimprint lithography,[5,6] block copolymer lithography,[7−15] and, recently, area-selective deposition (ASD).[16−18] Such methods are favorable in enabling future device integration and help alleviate fabrication demands, for example, litho-etch−litho-etch.

In particular, the ability of ASD to selectively include diverse material sets including oxides, dielectrics, and metals provides a route to produce material patterns and reduce the number of processing steps. The capacity of ASD to produce uniform metal and oxide layers can assist in the development of silicon device technologies,[19] and ASD is promising for implementation and cost reduction in fields beyond complementary metal−oxide−semiconductor (CMOS) processing, where stacked or patterned layers are required, for example, energy-harvesting surfaces[20] and catalysis.[21]

Various innovative ASD approaches have been reported and are typically based on self-assembled monolayers (SAMs) and atomic layer deposition (ALD) or molecular layer deposition. Others have examined unreactive polymeric resist layers combined with ALD of metal and dielectric films. For example, Leskelä *et al.* designed an approach using patterned SAMs to

Received: August 24, 2020
Published: October 6, 2020

https://dx.doi.org/10.1021/acs.langmuir.0c02512
Langmuir 2020, 36, 12394−12402

generate features on copper and silicon substrates[22−24] as well as patterned organic films for activation[25,26] and deactivation[27,28] layers with various ALD depositions (Ru, Ir, Pt, Al_2O_3, and TiO_2). Bent *et al.* have championed SAM use to mask and pattern copper lines on silicon[29,30] and several other substrate materials[31−35] together with ALD metallization. Furthermore, the Bent group has demonstrated a process for topographic selective anisotropic deposition of platinum *via* ALD by deactivating horizontal regions with (ion-implanted) fluorocarbons.[36] More recent ASD research has used ASD solely to fabricate defined materials at site-specific areas. For instance, Kessels and co-workers have incorporated area-selective ALD approaches that use organic inhibitors with ALD precursors,[37] surface activation *via* reactive plasma micropatterning,[38] and tuning of the oxygen ALD cycle exposure to selectively nucleate platinum on wafer regions.[39] The research has been extended to area-selective ALD on graphene surfaces (resist-free)[40] and ASD of ZnO by area activation using electron beam-induced deposition.[41] Kessels and co-workers have used ALD with catalytic oxygen activation of noble-metal surfaces[42] using a triple-step ALD cycle with a selective organic inhibitor, a precursor, and reactive plasma.[43] The group has also demonstrated selective deposition of ruthenium on the Pt/SiO_2 line space using ALD and atomic layer etching (ALE) cycles.[44] Parsons *et al.* have demonstrated selective deposition of diverse material sets (e.g., Ru, TiN, TiO_2, and HfO_2) *via* ALD on silicon nitride and silicon substrates by deactivating wafer areas with SAMs[45] using patterned amorphous carbon[46] and by exploiting inherent substrate selectivity.[47−49] They have also developed a TiO_2 ASD approach using ALD/ALE cycles.[50] More recently, Bates *et al.* introduced precise design rules for a new ASD technique known as "spin dewetting" that exploits modification of surface energies of line-space patterns.[51,52] Selectivity is induced by tuning polymer design to promote preferential dewetting from one substrate material and uniform wetting on the other.

Our previous work demonstrated the feasibility of covalently grafting polymer brush films to selectively deactivate the patterned Cu/SiO_2 line space for ASD of metal layers.[53] We demonstrated rapid grafting of reactive polymer brush films and subsequent conversion to various oxides (Al_2O_3,[54] Co_3O_4,[55] and CuO[56,57]) *via* liquid-phase metal-ion insertion. Liquid-phase deposition of metal ions on grafted brushes has many benefits because of the multitude of readily available, low-cost, and easily prepared (water-soluble) salt precursors. However, developing a vapor-phase brush infiltration approach can be beneficial for a wide array of applications, both ASD and blanket layers in the semiconductor industry. Moreover, achieving dense inorganic films in a simple one-step inclusion method at low temperatures is very appealing for industrial demands. TiO_2 films are routinely fabricated by sol−gel,[58] pulsed laser deposition (PVD),[59] chemical vapor deposition (CVD),[60] and ALD.[61,62] Significantly, a vapor-phase inclusion technique can deposit uniform ultrathin films compared to relatively high-temperature routes such as CVD and PVD. Evaporation and CVD-based techniques cannot achieve high-quality two-dimensional nanofilms with precise thickness control over large areas.[63]

In this article, a proof-of-concept technique for vapor-phase infiltration of covalently grafted polymer brushes to produce wafer-scale (>2 cm^2) TiO_2 with high uniformity is demonstrated on Si substrates. To fabricate coherent inorganic films with precise thickness control, it is critical to generate high-quality polymer brush films, that is, a complete monolayer. The definition of a polymer monolayer with complete coverage can be achieved and is straightforward for polymers which are weakly interacting with one another and the substrate (apart from the reactive terminal group used for grafting). Creating a complete monolayer is considerably more challenging for reactive systems with metal binding sites such as hydroxy-terminated poly-2-vinyl pyridine (P2VP-OH). The crucial parameters necessary for grafting poly-2-vinyl pyridine (P2VP) monolayers from the liquid phase with very high coverage and uniformity are explored. Factors such as polymer molecular weight (4−16 kg mol^{-1}), concentration of the casting solution (0.01−6 wt %), and quantity of end groups (monohydroxy-/dihydroxy-terminated) are examined (see Table 1). Finally, the potential of a hydroxy-terminated polystyrene (PS-OH) brush for substrate deactivation by limiting titanium tetraisopropoxide (TTIP) infiltration is highlighted. Precisely controlling polymer brushes for activating (P2VP-OH) and deactivating (PS-OH) semiconductor surfaces is a critical milestone for fulfilling future device scaling and three-dimensional (3D) architectures. The techniques discussed herein can have considerable importance because of the low process temperature (<500 °C) needed for CMOS fabrication.[64] The fundamental insights obtained can illuminate ways to utilize polymer brush films for vapor-phase film and ASD device-fabrication strategies.

Table 1. Polymer Properties and Annealing Conditions

polymer	M_n (kg mol^{-1})	end group (−OH)	annealing conditions
P2VP-OH	4.0	mono/di	60 s (230 °C)
	6.2	mono	60 s (230 °C)
	10.0	mono	60 s (230 °C)
	16.0	mono	60 s (230 °C)
PS-OH	6.0	mono	60 s (150 °C)
	10.0	mono	60 s (150 °C)
	16.0	mono	60 s (150 °C)
PMMA-OH	6.3	mono	90 s (190 °C)

EXPERIMENTAL SECTION

Materials. *Functionalized Polymers.* P2VP-OH: 4 kg mol^{-1} (P18796-2VPOH) [polydispersity index (PDI): 1.06], 6.2 kg mol^{-1} (P7544-2VPOH) (PDI: 1.05), 9.6 kg mol^{-1} (P19125-2VPOH) (PDI: 1.07), 16 kg mol^{-1} (P19128-2VPOH) (PDI: 1.11); dihydroxy-terminated P2VP: 4 kg mol^{-1} (P18798-2VPOH) (PDI: 1.06); hydroxy-terminated poly(methyl methacrylate) (PMMA-OH): 6.3 kg mol^{-1} (P1763-MMAOH) (PDI: 1.06); PS-OH: 6 kg mol^{-1} (P11116-SOH) (PDI: 1.05), 10 kg mol^{-1} (P18787-SOH) (PDI: 1.09), 16 kg mol^{-1} (P13135-SOH) (PDI: 1.09). The polymers have glass-transition temperatures of T_g = 95, 91, and 85 °C for PS-OH, P2VP-OH, and PMMA-OH, respectively.

Homopolymers. P2VP (P41306-2VP) (PDI: 1.04); polystyrene (P9405-S) (PDI: 1.03). All polymers were purchased from Polymer Source (Canada) and used without further purification.

Solvents. Tetrahydrofuran (THF) (inhibitor-free), toluene (Merck, Ireland) of high-performance liquid chromatography grade, and deionized water (ρ = 18.2 MΩ cm) were used as received.

Precursor. TTIP (99.999%) (Merck, Ireland) was used as received.

Pure P2VP, Polystyrene, Poly(methyl methacrylate), and SiO_2 Reference Substrates. Unfunctionalized P2VP, polystyrene (PS), and poly(methyl methacrylate) (PMMA) homopolymers were used to fabricate reference substrates. The powders were each dry-pressed into disc-shaped pellets (≈2 mm thick) at 350 MPa in a 13 mm diameter steel pellet die (Specac, a 13 mm evacuable pellet die).

https://dx.doi.org/10.1021/acs.langmuir.0c02512
Langmuir 2020, 36, 12394−12402

The pellets were exposed to solvent vapors (THF for P2VP and toluene for PS and PMMA) until a smooth mirrorlike surface was produced, similar to our previous work.[54] These fabricated substrates were used to determine the baseline contact angles (CAs) for pure polymer surfaces to infer brush coverage on Si substrates. Plasma-cleaned SiO_2 was used as a reference (60 s, 40 kHz, 50 W, Barrel Asher).

Polymer Brush Grafting. Silicon substrates (with a native oxide) were cleaned and hydroxyl-functionalized using an oxygen plasma treatment for 60 s (40 kHz, 50 W, Barrel Asher). P2VP-OH was dissolved in THF, and PMMA-OH and PS-OH were dissolved in toluene by stirring at room temperature (12 h). Polymer−solvent casting solutions were prepared at concentrations ranging from 0.01 to 6 wt % and spin-coated at 3000 rpm for 30 s. Samples were placed on a hot plate and annealed at 150 °C for 60 s (PS-OH), 190 °C for 90 s (PMMA-OH), and 230 °C for 60 s (P2VP-OH) for covalent grafting on SiO_2 *via* condensation reactions.[65,66] Figure S1 shows thermogravimetric analysis (TGA) showing maximum process temperatures for each polymer. Following baking periods, samples were sonicated in the respective solvents for 20 min (2 × 10 min washes) to remove the physisorbed, ungrafted polymer material.

Titanium Dioxide Fabrication. For the TTIP infiltration process, grafted monolayer films of 0.2 wt % P2VP (4 and 6 kg mol^{-1}) and 0.2 wt % PS were used (6 kg mol^{-1}). Samples were placed upside-down in a sealed glass chamber (height: 50 mm, diameter: 24 mm) containing ≈1 mL of TTIP for 2 h at 20 °C (partial pressure ≈ 53 Pa).[67] Polymer ashing and conversion to titanium dioxide were achieved by UV/ozone exposure (3 h) (Novascan PDSP-UV4).

Characterization. Field emission scanning electron microscopy (FESEM, Carl Zeiss Ultra) was performed using a secondary electron detector (InLens) with an accelerating voltage 1−2 kV. Focused ion beam etching (FIB, Helios NanoLab 460) was used for preparing a lamella specimen using standard high kilovolt milling and a low kilovolt final polish, and this rendered the lamella electron transparent, indicating an appropriate thickness for transmission electron microscopy (TEM). A capping layer of e-beam platinum (∼100 nm) and ion-beam Pt (∼2 μm) was used for FIB lamella. TEM (FEI Osiris) was performed using bright-field and scanning TEM (STEM) imaging. During STEM, the detector lengths were 220, 550, and 770 mm. The accelerating voltage was 200 kV. The energy-dispersive X-ray (EDX) beam current was 1 nA, and the acquisition time was 30 min. Atomic force microscopy (AFM, Park Systems XE7) was used with a noncontact cantilever (AC160TS, force constant ≈ 26 Nm^{-1}, resonant frequency ≈ 300 kHz).

X-ray photoelectron spectroscopy (XPS, VG Scientific ESCALAB Mk II) was performed under ultrahigh vacuum conditions (<5 × 10^{-10} mbar) using a hemispherical analyzer and Al Kα X-rays (1486.7 eV). The emitted photoelectrons were collected at a takeoff angle of 90° from the sample surface. The analyzer pass energy was set to 100 eV for survey scans and 20−40 eV for high-resolution core scans, yielding an overall resolution of 1.5 eV. Photoemission peak positions were corrected to C 1s at a binding energy of 284.8 eV.[68]

Dynamic CA measurements (a custom-built system) were recorded on five different regions of each sample using a high-speed camera (a 60 Hz sampling rate) to capture the advancing and receding CAs of three probe liquids (water, diiodomethane, and glycerol). Liquids were dispensed with a flow rate of 5 nL s^{-1} using a 35 gauge needle (a Ø135 μm optical density) with droplet volumes between 40 and 100 nL. Surface energy analysis was performed from the advancing CAs of the three probe liquids using the Lifshitz−van der Waals/acid−base approach.[69]

Dynamic light scattering (DLS, Malvern Zetasizer Nano ZSP) was performed on the polymer casting solutions.

TGA (Pyris 1) was performed on the functionalized polymers at a temperature range of 25−700 °C for 90 min.

RESULTS AND DISCUSSION

Monolayer Point of a Grafted Polymer Brush. We choose P2VP-OH (Figure 1a) because of the strong metal−

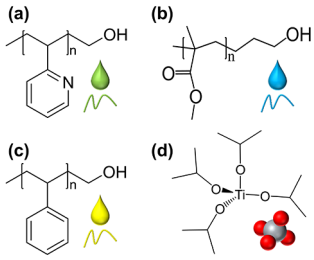

Figure 1. Chemical structures of the polymers and the inorganic material studied here include hydroxy-terminated (a) P2VP, (b) PMMA, and (c) PS and (d) TTIP.

pyridine binding interactions observed for a myriad of metal ions including Ti.[70,71] We have compared grafting parameters to those of another reactive polymer, PMMA-OH (Figure 1b), and a relatively nonreactive polymer, PS-OH (Figure 1c). The high-quality grafted P2VP brushes were exposed to vapor-phase TTIP (Figure 1d). Conversion to TiO_2 is performed using UV/ozone processing. Control over the final oxide thickness (≈2−4 nm) is demonstrated by adjusting the polymer molecular weight. This organometallic precursor (and the component of the Sharpless epoxidation) was chosen for its ability to selectively deposit Ti^{4+} cations within the hydrophilic domains of self-assembled block copolymers in our previous work.[72]

The Hansen approach was used to identify selective polymer−solvent casting solutions (P2VP/THF and PS/toluene) and is described in detail elsewhere.[54] Figure 2

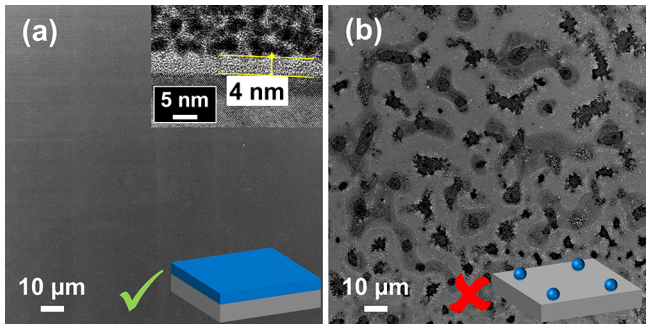

Figure 2. SEM image of a grafted P2VP-OH (M_n = 6 kg mol^{-1}) cast (a) below the CAC (with the TEM image in the inset) showing a uniform monolayer and (b) above the CAC with uneven coverage.

shows examples of the 6 kg mol^{-1} P2VP-OH polymer grafted from solutions of solvents above and below the critical agglomerate concentration (CAC) to silicon substrates. The SEM image in Figure 2a is characteristic of a well-grafted brush monolayer, cast from a 0.2 wt % solution. Figure S2 shows higher-magnification SEM images. The TEM image in Figure 2a (inset) shows that the brush film has high uniformity and a thickness of ≈4 nm (see Figure S3 for TEM of the 4 kg mol^{-1} grafted monolayer of ≈3.4 nm). By contrast, the SEM image in Figure 2b cast from a 2.0 wt % solution is an example of a poorly grafted P2VP-OH film with a molecular weight of 6.2 kg mol^{-1}. Polymer coverage is uneven and shown in more detail in Figure S4. The uneven nature of the P2VP-OH material shown in Figure 2b suggests that ideal conditions are not satisfied to define the observed structure as a brush film.

Dihydroxy-terminated P2VP (M_n = 4 kg mol^{-1}) was end-grafted, but uniform monolayer coverage was not achieved (see

https://dx.doi.org/10.1021/acs.langmuir.0c02512
Langmuir 2020, 36, 12394−12402

Figure S5a). Large agglomerates are present throughout the film, consistent with hydroxy end groups grafting to adjacent polymer end groups during annealing. We also note that the P2VP-OH polymer with molecular weights of 10 and 16 kg mol^{-1} did not form uniform monolayers (Figure S5b,c). DLS studies were performed on the casting solutions to elucidate the impact of concentration and molecular weight on the grafting mechanism. DLS of P2VP-OH (M_n = 6 kg mol^{-1}) casting solutions shows an increase in agglomerate size with concentration (Figure S6a,b). Figure S6c shows an increase in agglomerate size with molecular weight at a fixed concentration (0.2 wt %). The increase in agglomerate size in the casting solutions with concentration or molecular weight is consistent with the particularly strong pyridine−pyridine stacking interactions of the P2VP molecular system.[73] Figure 3 shows

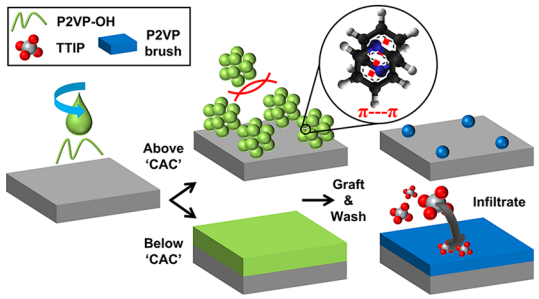

Figure 3. Schematic representation of the grafting process above and below the CAC for P2VP-OH (molecular weight: 6 kg mol^{-1}). Poor coverage occurs above the CAC because of strong pyridine−pyridine stacking interactions. The P2VP monolayer brush can be infiltrated with TTIP and converted to TiO_2 with a sub-5 nm thickness using UV/ozone.

a schematic of the proposed grafting mechanism above and below the CAC. As the casting solution concentration or polymer molecular weight increases, larger-sized agglomerates deposit on the substrate following spin coating. Above the CAC, the agglomerates are sufficiently large that steric repulsion effects begin to prevent the formation of a uniform coating, that is, gaps develop between agglomerates. Upon annealing, the chains near the substrate reptate and successfully locate the surface to overcome the thermodynamic reaction barrier to condensation. As the size of grafted polymer chains approaches the distance between adjacent grafting sites, the grafted chains overlap and transition between a single grafted chain and a brush regime.[74] The physisorbed overlayers are removed during the solvent wash to reveal an uneven coating. Below the CAC, a uniform brush monolayer can be prepared for TTIP vapor infiltration.

Figure 4 shows optimization data used to determine the monolayer point for grafting 4 kg mol^{-1} and 6 kg mol^{-1} P2VP-OH to silicon substrates. Solutions (0.01−6 wt %) were cast and grafted *via* baking, and the advancing water CA (WCA) measurements were immediately recorded, as shown in Figure 4a. The control reference SiO_2 sample has an average advancing WCA of θ_{SiO_2} = 4.0 ± 0.4°. At 0.01 wt %, the average advancing WCA increases to $\theta_{P2VP(4k)}$ = 47.4 ± 0.8° and $\theta_{P2VP(6k)}$ = 57.1 ± 2.6°, respectively. Above 0.05 wt %, the advancing WCAs rapidly asymptote and saturate with an average advancing WCA of $\theta_a \approx 77°$, similar to the value obtained for the pressed P2VP pellet ($\theta_{P2VP(max)}$ = 76.7 ± 1.6°). This trend holds for the 4 kg mol^{-1} polymer; however, above a concentration of ≈1 wt %, the 6 kg mol^{-1} P2VP-OH polymer rapidly transitions to a highly wetting surface ($\theta_{P2VP(6k)} < 10°$), consistent with the very low grafting density.

The observed θ_a behavior of the P2VP-OH brush surfaces is correlated to surface coverage using the Cassie−Baxter equation[75,76] with the assumption of surface energy heterogeneity at the molecular scale[77]

$$\Phi = \left(\frac{\cos\theta_{conc}}{\cos\theta_{SiO_2}} - 1\right) \Big/ \left(\frac{\cos\theta_{P2VP(max)}}{\cos\theta_{SiO_2}} - 1\right) \quad (1)$$

where Φ is the apparent surface coverage of the grafted polymer brush, θ_{conc} is θ_a measured at a given grafting concentration, and $\theta_{P2VP(max)}$ is θ_a of the pure P2VP pellet. Figure 4b shows the change of surface coverage with solution concentration for the brush samples, calculated from eq 1. The increased Φ at the low dilution limit (0.01 wt %) for the 6 kg mol^{-1} versus 4 kg mol^{-1} P2VP-OH brush is consistent with a longer chain length, that is, more surface coverage for equivalent condensation reactions. Additionally, we used XPS in order to provide further confirmation of the grafting behavior of the 4 kg mol^{-1} and 6 kg mol^{-1} P2VP-OH systems. The N 1s signal (~401 eV) from grafted brushes was tracked over the concentration range in Figure 4c. A strikingly similar evolution profile to Figure 4a,b is observed from the N 1s data, consistent with the coverage level determined by the WCA and the Cassie−Baxter equation. Figure 4d−f shows AFM images of the 4 kg mol^{-1} P2VP-OH-grafted brush (0.2, 2.0, and 6.0 wt %). The films are very smooth with high coverage, with a root-mean-square (rms) roughness of ≈ 0.6 nm (the average of three AFM scans). The roughness factor *r*, defined as the ratio of actual surface area to projected area, was calculated from the height images <1.04, representing minimal contribution to surface wettability as per the Wenzel equation, $\cos\theta_{apparent} = r \cos\theta$.[78] For the 6 kg mol^{-1} brush (Figure 4g−i), only the film cast from a 0.2 wt % solution shows good uniformity and coverage. Figure S7 shows detailed surface energy analysis of the grafted brushes. At high coverage, the dispersive and polar components match those of the pure polymer pellet and the silicon control at low coverage (Figure S7a). The same trend is observed for the Lewis acid and Lewis base interactions (Figure S7b). Grafting kinetics experiments were performed at lower temperatures for the polymers and reported in our previous work.[54]

The grafting process was tested with PS-OH (M_n = 6.0−16.0 kg mol^{-1}), as shown in Section S2. Grafting high-quality uniform monolayers was achievable at all molecular weights and concentrations (>0.01 wt %). PMMA-OH (M_n = 6.3 kg mol^{-1}) was tested (Section S3) with high-quality monolayers observed even for 6.0 wt % grafting solutions. These less reactive brushes can graft monolayers at a higher molecular weight and concentration compared with polyvinylpyridine (PVP), where stronger intermolecular forces exist between the molecules because of substantial π-orbital interactions.[73] Casting at elevated temperature, or using a more selective solvent, is also a possible route to high-molecular-weight PVP-based monolayer films. Further characterization techniques such as small-angle neutron scattering and small-angle X-ray scattering can help elucidate the chain conformation in the polymer brush[79] and will be reported in due course.

Polymer Brush Exposure/Infiltration to Titanium Isopropoxide. The optimized 4 kg mol^{-1} and 6 kg mol^{-1} P2VP-OH brush monolayers were exposed to TTIP vapors

https://dx.doi.org/10.1021/acs.langmuir.0c02512
Langmuir 2020, 36, 12394−12402

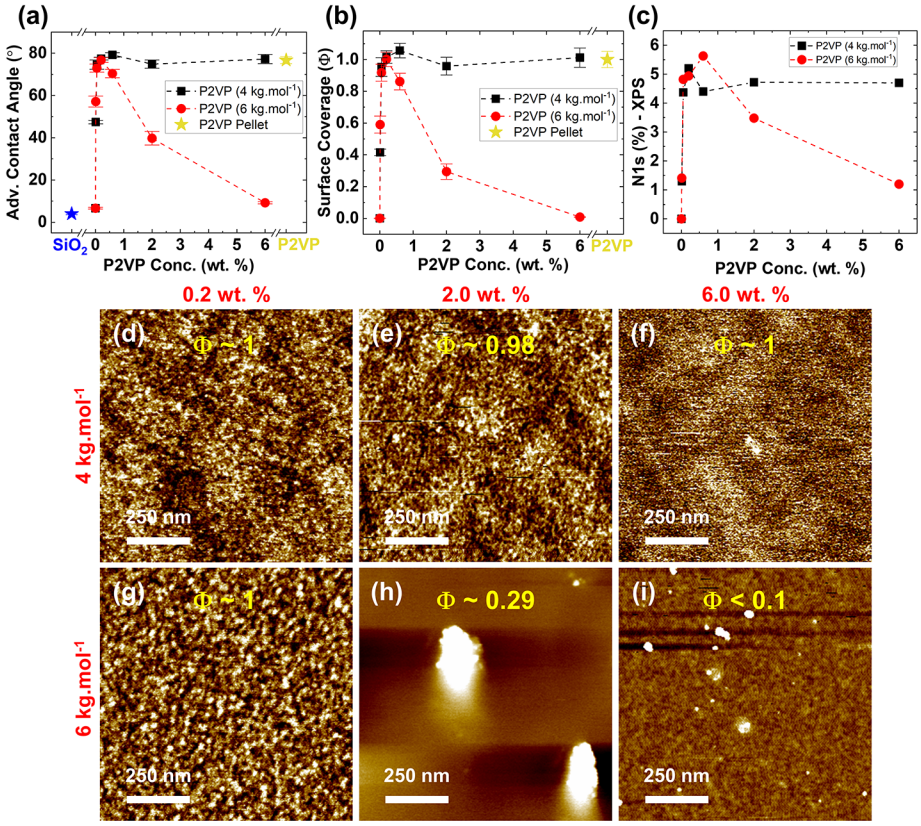

Figure 4. (a) Advancing WCAs of the 4 kg mol^{-1} and 6 kg mol^{-1} P2VP brush samples grafted on silicon substrates over a range of concentrations with corresponding coverage (b). (c) XPS nitrogen (N 1s) atomic percentage of the grafted polymers as a function of concentration. AFM topographic images of the P2VP brushes grafted from 0.2 to 6 wt % solutions for (d–f) 4 kg mol^{-1} and (g–i) 6 kg mol^{-1} P2VP-OH.

and converted to TiO_2 films (see the Experimental Section for TTIP infiltration conditions). The Ti 2p XPS spectra in Figure 5a show the TTIP-infiltrated brushes and their conversion to TiO_2. Both brushes were treated under the same TTIP processing conditions; however, an ≈50% more precursor uptake is measured in the 6 kg mol^{-1} brush. Figure S15 shows the corresponding survey spectra showing an increase in the Ti signal from 6.2 to 9.0%. TiO_2 is formed after UV/ozone exposure with the Ti $2p_{3/2}$ and Ti $2p_{1/2}$ peaks at ≈458 and 464 eV, respectively.[80] A slight reduction in the Ti signal occurs following ashing because of partial removal of the TTIP precursor. The O 1s spectra in Figure 5b display the TTIP-infiltrated P2VP-OH brush (M_n = 6.2) before and after UV/ozone exposure. Before and after UV/ozone exposure, the Si–O and Ti–O peaks are observed at ≈532.7 and ≈530.7 eV, respectively, consistent with literature values.[81,82] Post UV/ozone exposure, there is an increase in the SiO_2 peak because of reduced attenuation of the substrate signal. Before UV/ozone exposure, the N 1s region (Figure 5c) has a peak at ≈399 eV associated with C=N–C pyridine bonds,[83,84] while after UV/ozone exposure, the pyridine signal is absent (within XPS detection limits), indicating total removal/conversion of the brush material.

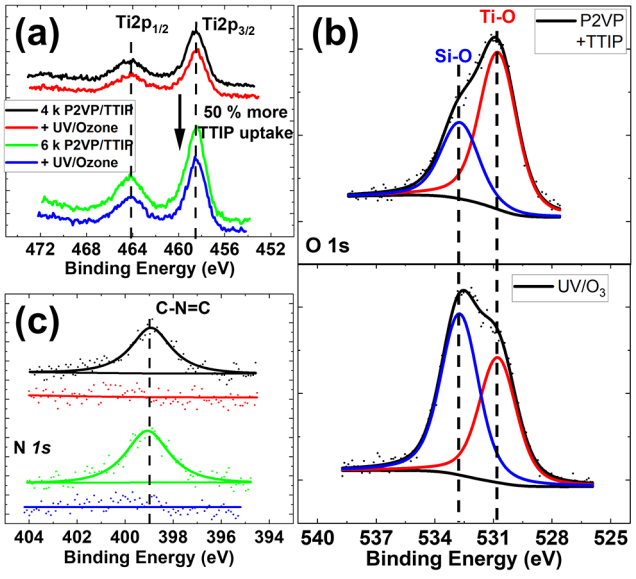

Figure 5. XPS high-resolution spectra (raw counts) of grafted 4 kg mol^{-1} and 6 kg mol^{-1} P2VP-OH brushes exposed to TTIP and following UV/ozone exposure for (a) titanium 2p, (b) oxygen 1s, and (c) nitrogen 1s.

The TEM image in Figure 6a shows a TiO_2 film (≈4 nm thick) produced using a 6 kg mol^{-1} P2VP-OH brush. EDX elemental maps in Figure 6b show the film with titanium and oxygen signals present. Figure S16 shows the film before UV/ozone exposure, and Figures S17 and S18 show the process applied to the 4 kg mol^{-1} P2VP-OH brush. Moreover, a thinner TiO_2 film (≈2 nm) is fabricated using the 4 kg mol^{-1} brush, showing that our process can be used to tune TiO_2 films with nanometer control. For comparison, the TTIP infiltration process was applied to the 6 kg mol^{-1} PS-OH grafted brush (Figure S19). PS-OH-grafted brushes exhibit excellent

https://dx.doi.org/10.1021/acs.langmuir.0c02512
Langmuir 2020, 36, 12394–12402

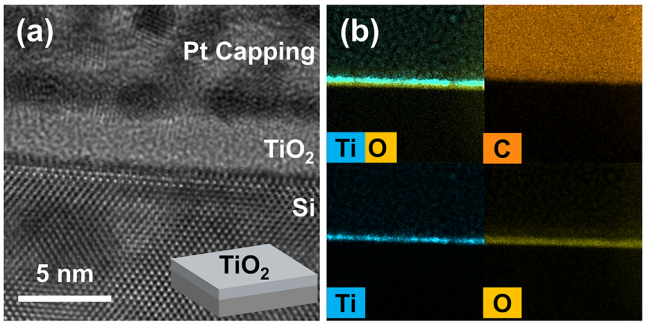

Figure 6. (a) Bright-field TEM image of the titanium dioxide film (after UV/ozone exposure) and (b) corresponding EDX maps (Ti, C, and O) following TTIP treatment of a uniform P2VP-OH brush film (M_n = 6 kg mol^{-1}). The TiO_2 thickness is 4 nm.

potential for blocking TTIP infiltration, with EDX maps confirming that the precursor is inhibited by the PS brush with no Ti present at the substrate interface. The TTIP infiltration process can be further optimized by developing a vapor annealing chamber to precisely control precursor saturation conditions. Titanium is an attractive model species for vapor-phase brush infiltration given its use in a variety of far-reaching applications, for example, TiO_2 coatings are widely used in self-cleaning technologies,[85] as an electrode support,[86] as a dielectric medium,[87] and in photocatalysis.[88] ALD-grown TiO_2 nanofilms have been used in many applications: corrosion protection layers on copper,[89] high-κ dielectrics, solar cells (perovskite),[90] carbon nanotubes,[91] and composite nanostructures for water splitting to name a few.[92]

CONCLUSIONS

High-quality TiO_2 films were fabricated using a simple apparatus that allowed the definition of precise polymer films for hosting titanium precursors using a facile vapor-phase infiltration technique. It was shown that high-coverage, pin hole-free, homogeneous TiO_2 films with a tunable thickness could be produced, as confirmed by extensive SEM and TEM analysis. We have established the precise parameters required for end-grafting monolayer P2VP-OH polymer brushes (i.e., polymer molecular weight, casting solution concentration, and terminal group density). The brush layer deposition/attachment requires careful optimization to allow monolayer formation, which subsequently facilitates the regularity of the inorganic film. As the P2VP brushes contain active groups that bind to the metal, there is a propensity for coordination of the polymer to form aggregates in solution and 3D films that mitigate against precise monolayer formation. This work shows that process conditions and treatments can be created to mitigate these difficulties.

A vapor-phase approach involving Ti precursor inclusion into monolayer brush films was demonstrated on grafted P2VP-OH. A grafting comparison of P2VP with PS and PMMA highlights the strong pyridine-stacking interactions that inhibit film formation above the CAC. The results show that the initial polymer films need very careful tuning for developing uniform inorganic films. High-quality grafted P2VP-OH brushes were exposed to vapor-phase TTIP, and conversion to TiO_2 is performed using UV/ozone processing, as confirmed by XPS and EDX characterization. Control over the final oxide thickness (≈2−4 nm) is demonstrated by adjusting the polymer molecular weight. One should note that although P2VP is an ideal system for metal incorporation, developing thicker films with PVP brushes is quite prohibitive because of strong intermolecular forces. Therefore, less reactive brushes such as PMMA may be more suitable for fabricating thick inorganic films, and studies are currently underway. In parallel, we have shown that PS brushes demonstrate excellent potential for surface deactivation, where TTIP deposition was completely prevented from reaching the substrate. In summary, we precisely controlled polymer brushes for activating (P2VP-OH) and deactivating (PS-OH) semiconductor surfaces, which is a first achievement of this critical milestone for fulfilling future device scaling and 3D architectures. We envisage that our deposition and brush process could also find use in other sectors that rely on uniform nanometer inorganic films, for example, glass coating technologies (self-cleaning, anticondensation, low emissivity, etc.), digital display (electrode and conductive and emissive LCD/LED/OLED layers).

ASSOCIATED CONTENT

Supporting Information

The Supporting Information is available free of charge at https://pubs.acs.org/doi/10.1021/acs.langmuir.0c02512.

Grafting data for PS-OH and PMMA-OH and additional XPS, EDX, AFM, and electron microscopy data (PDF)

AUTHOR INFORMATION

Corresponding Authors

Ross Lundy − *AMBER Research Centre and School of Chemistry, Trinity College Dublin, Dublin 2, Ireland;* orcid.org/0000-0002-1329-8614; Email: ross.lundy2@gmail.com

Michael A. Morris − *AMBER Research Centre and School of Chemistry, Trinity College Dublin, Dublin 2, Ireland;* orcid.org/0000-0001-8756-4068; Email: morrism2@tcd.ie

Authors

Pravind Yadav − *AMBER Research Centre and School of Chemistry, Trinity College Dublin, Dublin 2, Ireland*

Nadezda Prochukhan − *AMBER Research Centre and School of Chemistry, Trinity College Dublin, Dublin 2, Ireland;* orcid.org/0000-0002-2535-7132

Elsa C. Giraud − *AMBER Research Centre and School of Chemistry, Trinity College Dublin, Dublin 2, Ireland;* orcid.org/0000-0002-8556-570X

Tom F. O'Mahony − *AMBER Research Centre and School of Chemistry, Trinity College Dublin, Dublin 2, Ireland*

Andrew Selkirk − *AMBER Research Centre and School of Chemistry, Trinity College Dublin, Dublin 2, Ireland;* orcid.org/0000-0002-1845-7100

Eleanor Mullen − *AMBER Research Centre and School of Chemistry, Trinity College Dublin, Dublin 2, Ireland*

Jim Conway − *National Centre for Plasma Science and Technology, Dublin City University, Dublin 9, Ireland*

Miles Turner − *National Centre for Plasma Science and Technology, Dublin City University, Dublin 9, Ireland*

Stephen Daniels − *National Centre for Plasma Science and Technology, Dublin City University, Dublin 9, Ireland*

P. G. Mani-Gonzalez − *Institute of Engineering and Technology, Department of Physics and Mathematics, Autonomous*

https://dx.doi.org/10.1021/acs.langmuir.0c02512
Langmuir 2020, 36, 12394−12402

University of Ciudad Juárez, Cd. Juárez 32310, Mexico; orcid.org/0000-0001-6993-2349

Matthew Snelgrove − *School of Physical Sciences, Dublin City University, Dublin 9, Ireland;* orcid.org/0000-0003-0344-1146

Justin Bogan − *School of Physical Sciences, Dublin City University, Dublin 9, Ireland;* orcid.org/0000-0001-9483-0299

Caitlin McFeely − *School of Physical Sciences, Dublin City University, Dublin 9, Ireland*

Robert O'Connor − *School of Physical Sciences, Dublin City University, Dublin 9, Ireland*

Enda McGlynn − *National Centre for Plasma Science and Technology and School of Physical Sciences, Dublin City University, Dublin 9, Ireland*

Greg Hughes − *National Centre for Plasma Science and Technology and School of Physical Sciences, Dublin City University, Dublin 9, Ireland*

Cian Cummins − *AMBER Research Centre and School of Chemistry, Trinity College Dublin, Dublin 2, Ireland;* orcid.org/0000-0001-6338-3991

Complete contact information is available at: https://pubs.acs.org/10.1021/acs.langmuir.0c02512

Author Contributions

⊥R.L. and P.Y. contributed equally.

Notes

The authors declare no competing financial interest.

■ ACKNOWLEDGMENTS

We gratefully acknowledge the work of Alan Bell, Chris O'Neill, and David Bird in Intel Analytical Labs for providing technical assistance with TEM imaging and sample preparation. We thank Matt Shaw, Jennifer McKenna, and Alan Bell (Intel) for technical advice and discussions. R.L. gratefully acknowledges the staff of the Advanced Microscopy Laboratory (AML), Trinity College Dublin, for their assistance during characterization. This publication has emanated from research conducted with the financial support of Science Foundation Ireland (SFI) under grant numbers 12/RC/2278 and 16/SP/3809. This research is also cofunded by the European Regional Development Fund and SFI under Ireland's European Structural and Investment Fund.

■ REFERENCES

(1) Morris, M. A. Directed Self-Assembly of Block Copolymers for Nanocircuitry Fabrication. *Microelectron. Eng.* **2015**, *132*, 207−217.

(2) Samsung Electronics' Leadership in Advanced Foundry Technology Showcased with Latest Silicon Innovations and Ecosystem Platform. https://news.samsung.com/global/samsung-electronics-leadership-in-advanced-foundry-technology-showcased-with-latest-silicon-innovations-and-ecosystem-platform (accessed Dec 3, 2019).

(3) TSMC starts work on US$19.6 Billion 3nm fab i. Taiwan News https://www.taiwannews.com.tw/en/news/3805032 (accessed Dec 3, 2019).

(4) Bae, G.; Bae, D. I.; Kang, M.; Hwang, S. M.; Kim, S. S.; Seo, B.; Kwon, T. Y.; Lee, T. J.; Moon, C.; Choi, Y. M.; et al. 3nm GAA Technology Featuring Multi-Bridge-Channel FET for Low Power and High Performance Applications. *Technical Digest-International Electron Devices Meeting, IEDM*; Institute of Electrical and Electronics Engineers Inc., 2019; Vol. *2018*, pp 28.7.1−28.7.4.

(5) Mårtensson, T.; Carlberg, P.; Borgström, M.; Montelius, L.; Seifert, W.; Samuelson, L. Nanowire Arrays Defined by Nanoimprint Lithography. *Nano Lett.* **2004**, *4*, 699−702.

(6) Borah, D.; Cummins, C.; Rasappa, S.; Senthamaraikannan, R.; Salaun, M.; Zelsmann, M.; Liontos, G.; Ntetsikas, K.; Avgeropoulos, A.; Morris, M.; et al. Nanopatterning via Self-Assembly of a Lamellar-Forming Polystyrene-Block-Poly(Dimethylsiloxane) Diblock Copolymer on Topographical Substrates Fabricated by Nanoimprint Lithography. *Nanomaterials* **2018**, *8*, 32.

(7) Cummins, C.; Mokarian-Tabari, P.; Andreazza, P.; Sinturel, C.; Morris, M. A. Solvothermal Vapor Annealing of Lamellar Poly-(Styrene)-Block-Poly(d,l-Lactide) Block Copolymer Thin Films for Directed Self-Assembly Application. *ACS Appl. Mater. Interfaces* **2016**, *8*, 8295.

(8) Ross, C. A.; Berggren, K. K.; Cheng, J. Y.; Jung, Y. S.; Chang, J.-B. Three-Dimensional Nanofabrication by Block Copolymer Self-Assembly. *Adv. Mater.* **2014**, *26*, 4386−4396.

(9) Oh, J.; Suh, H. S.; Ko, Y.; Nah, Y.; Lee, J.-C.; Yeom, B.; Char, K.; Ross, C. A.; Son, J. G. Universal Perpendicular Orientation of Block Copolymer Microdomains Using a Filtered Plasma. *Nat. Commun.* **2019**, *10*, 2912.

(10) Fernandez, E.; Tu, K.-H.; Ho, P.; Ross, C. A. Thermal Stability of L10-FePt Nanodots Patterned by Self-Assembled Block Copolymer Lithography. *Nanotechnology* **2018**, *29*, 465301.

(11) Tu, K.-H.; Bai, W.; Liontos, G.; Ntetsikas, K.; Avgeropoulos, A.; Ross, C. a. Universal Pattern Transfer Methods for Metal Nanostructures by Block Copolymer Lithography. *Nanotechnology* **2015**, *26*, 375301.

(12) Gotrik, K. W.; Hannon, A. F.; Son, J. G.; Keller, B.; Alexander-katz, A.; Ross, C. A. Morphology Control in Block Copolymer Films Using Mixed Solvent Vapors. *ACS Nano* **2012**, *6*, 8052.

(13) Lundy, R.; Flynn, S. P.; Cummins, C.; Kelleher, S. M.; Collins, M. N.; Dalton, E.; Daniels, S.; Morris, M. A.; Enright, R. Controlled Solvent Vapor Annealing of a High χ Block Copolymer Thin Film. *Phys. Chem. Chem. Phys.* **2017**, *19*, 2805−2815.

(14) Lundy, R.; Flynn, S. P.; Cummins, C.; Kelleher, S. M.; Collins, M. N.; Dalton, E.; Daniels, S.; Morris, M.; Enright, R. Nanoporous Membrane Production via Block Copolymer Lithography for High Heat Dissipation Systems. *2016 15th IEEE Intersociety Conference on Thermal and Thermomechanical Phenomena in Electronic Systems (ITherm)*; IEEE, 2016; pp 1267−1272.

(15) Cummins, C.; Lundy, R.; Walsh, J. J.; Ponsinet, V.; Fleury, G.; Morris, M. A. Enabling Future Nanomanufacturing through Block Copolymer Self-Assembly: A Review. *Nano Today* **2020**, *35*, 100936.

(16) Mackus, A. J. M.; Merkx, M. J. M.; Kessels, W. M. M. From the Bottom-Up: Toward Area-Selective Atomic Layer Deposition with High Selectivity †. *Chem. Mater.* **2019**, *31*, 2−12.

(17) Seo, S.; Yeo, B. C.; Han, S. S.; Yoon, C. M.; Yang, J. Y.; Yoon, J.; Yoo, C.; Kim, H.-j.; Lee, Y.-b.; Lee, S. J.; et al. Reaction Mechanism of Area-Selective Atomic Layer Deposition for Al2O3 Nanopatterns. *ACS Appl. Mater. Interfaces* **2017**, *9*, 41607−41617.

(18) Prasittichai, C.; Pickrahn, K. L.; Minaye Hashemi, F. S.; Bergsman, D. S.; Bent, S. F. Improving Area-Selective Molecular Layer Deposition by Selective SAM Removal. *ACS Appl. Mater. Interfaces* **2014**, *6*, 17831−17836.

(19) Nagata, T. *Material Design of Metal/Oxide Interfaces for Nanoelectronics Applications*, 1st ed.; Springer: Japan, 2020.

(20) Li, R.; Zhang, F.; Wang, D.; Yang, J.; Li, M.; Zhu, J.; Zhou, X.; Han, H.; Li, C. Spatial Separation of Photogenerated Electrons and Holes among {010} and {110} Crystal Facets of BiVO 4. *Nat. Commun.* **2013**, *4*, 1432.

(21) Xie, J.; Yang, X.; Han, B.; Shao-Horn, Y.; Wang, D. Site-Selective Deposition of Twinned Platinum Nanoparticles on $TiSi_2$ Nanonets by Atomic Layer Deposition and Their Oxygen Reduction Activities. *ACS Nano* **2013**, *7*, 6337−6345.

(22) Färm, E.; Kemell, M.; Ritala, M.; Leskelä, M. Self-Assembled Octadecyltrimethoxysilane Monolayers Enabling Selective-Area Atomic Layer Deposition of Iridium. *Chem. Vap. Deposition* **2006**, *12*, 415−417.

(23) Färm, E.; Kemell, M.; Ritala, M.; Leskelä, M. Selective-Area Atomic Layer Deposition with Microcontact Printed Self-Assembled Octadecyltrichlorosilane Monolayers as Mask Layers. *Thin Solid Films* **2008**, *517*, 972−975.
(24) Färm, E.; Vehkamäki, M.; Ritala, M.; Leskelä, M. Passivation of Copper Surfaces for Selective-Area ALD Using a Thiol Self-Assembled Monolayer. *Semicond. Sci. Technol.* **2012**, *27*, 074004.
(25) Färm, E.; Lindroos, S.; Ritala, M.; Leskelä, M. Microcontact Printed Films as an Activation Layer for Selective Atomic Layer Deposition. U.S. Patent 9,223,203 B2, July 8, 2011.
(26) Färm, E.; Lindroos, S.; Ritala, M.; Leskelä, M. Microcontact Printed RuO x Film as an Activation Layer for Selective-Area Atomic Layer Deposition of Ruthenium. *Chem. Mater.* **2012**, *24*, 275−278.
(27) Färm, E.; Kemell, M.; Ritala, M.; Leskelä, M. Selective-Area Atomic Layer Deposition Using Poly(Methyl Methacrylate) Films as Mask Layers. *J. Phys. Chem. C* **2008**, *112*, 15791−15795.
(28) Färm, E.; Kemell, M.; Santala, E.; Ritala, M.; Leskelä, M. Selective-Area Atomic Layer Deposition Using Poly(Vinyl Pyrrolidone) as a Passivation Layer. *J. Electrochem. Soc.* **2010**, *157*, K10.
(29) Minaye Hashemi, F. S.; Prasittichai, C.; Bent, S. F. Self-Correcting Process for High Quality Patterning by Atomic Layer Deposition. *ACS Nano* **2015**, *9*, 8710−8717.
(30) Minaye Hashemi, F. S.; Birchansky, B. R.; Bent, S. F. Selective Deposition of Dielectrics: Limits and Advantages of Alkanethiol Blocking Agents on Metal-Dielectric Patterns. *ACS Appl. Mater. Interfaces* **2016**, *8*, 33264−33272.
(31) Chen, R.; Kim, H.; McIntyre, P. C.; Bent, S. F. Self-Assembled Monolayer Resist for Atomic Layer Deposition of HfO2 and ZrO2 High-κ Gate Dielectrics. *Appl. Phys. Lett.* **2004**, *84*, 4017−4019.
(32) Chen, R.; Kim, H.; McIntyre, P. C.; Bent, S. F. Investigation of Self-Assembled Monolayer Resists for Hafnium Dioxide Atomic Layer Deposition. *Chem. Mater.* **2005**, *17*, 536−544.
(33) Hong, J.; Porter, D. W.; Sreenivasan, R.; McIntyre, P. C.; Bent, S. F. ALD Resist Formed by Vapor-Deposited Self-Assembled Monolayers. *Langmuir* **2007**, *23*, 1160−1165.
(34) Jiang, X.; Bent, S. F. Area-Selective ALD with Soft Lithographic Methods: Using Self-Assembled Monolayers to Direct Film Deposition. *J. Phys. Chem. C* **2009**, *113*, 17613−17625.
(35) Bobb-Semple, D.; Nardi, K. L.; Draeger, N.; Hausmann, D. M.; Bent, S. F. Area-Selective Atomic Layer Deposition Assisted by Self-Assembled Monolayers: A Comparison of Cu, Co, W, and Ru. *Chem. Mater.* **2019**, *31*, 1635−1645.
(36) Kim, W.-H.; Minaye Hashemi, F. S.; Mackus, A. J. M.; Singh, J.; Kim, Y.; Bobb-Semple, D.; Fan, Y.; Kaufman-Osborn, T.; Godet, L.; Bent, S. F. A Process for Topographically Selective Deposition on 3D Nanostructures by Ion Implantation. *ACS Nano* **2016**, *10*, 4451−4458.
(37) Vervuurt, R. H. J.; Sharma, A.; Jiao, Y.; Kessels, W.; Erwin, M. M.; Bol, A. A. Area-Selective Atomic Layer Deposition of Platinum Using Photosensitive Polyimide. *Nanotechnology* **2016**, *27*, 405302.
(38) Mameli, A.; Kuang, Y.; Aghaee, M.; Ande, C. K.; Karasulu, B.; Creatore, M.; Mackus, A. J. M.; Kessels, W. M. M.; Roozeboom, F. Area-Selective Atomic Layer Deposition of In $_2$ O $_3$:H Using a μ-Plasma Printer for Local Area Activation. *Chem. Mater.* **2017**, *29*, 921−925.
(39) MacKus, A. J. M.; Verheijen, M. A.; Leick, N.; Bol, A. A.; Kessels, W. M. M. Influence of Oxygen Exposure on the Nucleation of Platinum Atomic Layer Deposition: Consequences for Film Growth, Nanopatterning, and Nanoparticle Synthesis. *Chem. Mater.* **2013**, *25*, 1905−1911.
(40) Thissen, N. F. W.; Vervuurt, R. H. J.; Mackus, A. J. M.; Mulders, J. J. L.; Weber, J.-W.; Kessels, W. M. M.; Bol, A. A. Graphene Devices with Bottom-up Contacts by Area-Selective Atomic Layer Deposition. *2D Mater.* **2017**, *4*, 025046.
(41) Mameli, A.; Karasulu, B.; Verheijen, M. A.; Barcones, B.; Macco, B.; Mackus, A. J. M.; Kessels, W. M. M. E.; Roozeboom, F. Area-Selective Atomic Layer Deposition of ZnO by Area Activation Using Electron Beam-Induced Deposition. *Chem. Mater.* **2019**, *31*, 1250−1257.
(42) Singh, J. A.; Thissen, N. F. W.; Kim, W.-H.; Johnson, H.; Kessels, W. M. M.; Bol, A. A.; Bent, S. F.; Mackus, A. J. M. Area-Selective Atomic Layer Deposition of Metal Oxides on Noble Metals through Catalytic Oxygen Activation. *Chem. Mater.* **2018**, *30*, 663−670.
(43) Mameli, A.; Merkx, M. J. M.; Karasulu, B.; Roozeboom, F.; Kessels, W.; Erwin, M. M.; Mackus, A. J. M. Area-Selective Atomic Layer Deposition of SiO $_2$ Using Acetylacetone as a Chemoselective Inhibitor in an ABC-Type Cycle. *ACS Nano* **2017**, *11*, 9303−9311.
(44) Vos, M. F. J.; Chopra, S. N.; Verheijen, M. A.; Ekerdt, J. G.; Agarwal, S.; Kessels, W. M. M.; Mackus, A. J. M. Area-Selective Deposition of Ruthenium by Combining Atomic Layer Deposition and Selective Etching. *Chem. Mater.* **2019**, *31*, 3878−3882.
(45) Park, K. J.; Doub, J. M.; Gougousi, T.; Parsons, G. N. Microcontact Patterning of Ruthenium Gate Electrodes by Selective Area Atomic Layer Deposition. *Appl. Phys. Lett.* **2005**, *86*, 051903.
(46) Stevens, E.; Tomczak, Y.; Chan, B. T.; Altamirano Sanchez, E.; Parsons, G. N.; Delabie, A. Area-Selective Atomic Layer Deposition of TiN, TiO $_2$, and HfO $_2$ on Silicon Nitride with Inhibition on Amorphous Carbon. *Chem. Mater.* **2018**, *30*, 3223−3232.
(47) Atanasov, S. E.; Kalanyan, B.; Parsons, G. N. Inherent Substrate-Dependent Growth Initiation and Selective-Area Atomic Layer Deposition of TiO $_2$ Using "Water-Free" Metal-Halide/Metal Alkoxide Reactants. *J. Vac. Sci. Technol., A* **2016**, *34*, 01A148.
(48) Parsons, G. N.; Kalanyan, B.; Atanasov, S. E.; Lemaire, P.; Oldham, C. Using Inherent Substrate-Dependent Nucleation to Promote Metal and Metal Oxide Selective-Area Atomic Layer Deposition. *ECS Trans.* **2016**, *75*, 77−83.
(49) Parsons, G. N. Functional Model for Analysis of ALD Nucleation and Quantification of Area-Selective Deposition. *J. Vac. Sci. Technol., A* **2019**, *37*, 020911.
(50) Song, S. K.; Saare, H.; Parsons, G. N. Integrated Isothermal Atomic Layer Deposition/Atomic Layer Etching Super-Cycles for Area-Selective Deposition of TiO $_2$. *Chem. Mater.* **2019**, *31*, 4793.
(51) Zhang, Y.; Discekici, E. H.; Burns, R. L.; Somervell, M.; Hawker, C. J.; Bates, C. M. A Single-Step, Spin-on Process for High Fidelity and Selective Polymer Deposition. *ACS Appl. Polym. Mater.* **2019**, *2*, 481.
(52) Zhang, Y.; D'Ambra, C. A.; Katsumata, R.; Burns, R. L.; Somervell, M. H.; Segalman, R. A.; Hawker, C. J.; Bates, C. M. Rapid and Selective Deposition of Patterned Thin Films on Heterogeneous Substrates via Spin Coating. *ACS Appl. Mater. Interfaces* **2019**, *11*, 21177−21183.
(53) Cummins, C.; Weingärtner, T.; Morris, M. A. Enabling Large-Area Selective Deposition on Metal-Dielectric Patterns Using Polymer Brush Deactivation. *J. Phys. Chem. C* **2018**, *122*, 14698−14705.
(54) Lundy, R.; Yadav, P.; Selkirk, A.; Mullen, E.; Ghoshal, T.; Cummins, C.; Morris, M. A. Optimizing Polymer Brush Coverage To Develop Highly Coherent Sub-5 Nm Oxide Films by Ion Inclusion. *Chem. Mater.* **2019**, *31*, 9338−9345.
(55) Cummins, C.; Shaw, M. T.; Morris, M. A. Area Selective Polymer Brush Deposition. *Macromol. Rapid Commun.* **2017**, *38*, 1700252.
(56) Snelgrove, M.; Mani-Gonzalez, P. G.; Bogan, J.; Lundy, R.; Rueff, J. P.; Hughes, G.; Yadav, P.; McGlynn, E.; Morris, M.; O'Connor, R. Hard X-Ray Photoelectron Spectroscopy Study of Copper Formation by Metal Salt Inclusion in a Polymer Film. *J. Phys. D: Appl. Phys.* **2019**, *52*, 435301.
(57) Mani-Gonzalez, P. G.; Snelgrove, M.; Rueff, J.-P.; Lundy, R.; Yadav, P.; Bogan, J.; O'Connor, R.; Morris, M.; Hughes, G. Analysis of Al and Cu Salt Infiltration into a Poly 2- Vinylpyridine (P2vP) Polymer Layer for Semiconductor Device Patterning Applications. *J. Phys. D: Appl. Phys.* **2020**, *53*, 115105.
(58) Wang, C.-C.; Ying, J. Y. Sol-Gel Synthesis and Hydrothermal Processing of Anatase and Rutile Titania Nanocrystals. *Chem. Mater.* **1999**, *11*, 3113−3120.
(59) Major, B.; Ebner, R.; Ziba, P.; Wolczyski, W. Titanium-Based Films Deposited Using a Nd:YAG Pulsed Laser. *Appl. Phys. A: Mater. Sci. Process.* **1999**, *69*, S921.

https://dx.doi.org/10.1021/acs.langmuir.0c02512
Langmuir 2020, 36, 12394−12402

(60) Shi, J.; Wang, X. Growth of Rutile Titanium Dioxide Nanowires by Pulsed Chemical Vapor Deposition. *Cryst. Growth Des.* **2011**, *11*, 949−954.
(61) Klesko, J. P.; Rahman, R.; Dangerfield, A.; Nanayakkara, C. E.; L'Esperance, T.; Moser, D. F.; Peña, L. F.; Mattson, E. C.; Dezelah, C. L.; Kanjolia, R. K.; et al. Selective Atomic Layer Deposition Mechanism for Titanium Dioxide Films with (EtCp)Ti(NMe2)3: Ozone versus Water. *Chem. Mater.* **2018**, *30*, 970−981.
(62) Ritala, M.; Leskela, M.; Niinisto, L.; Haussalo, P. Titanium Isopropoxide as a Precursor in Atomic Layer Epitaxy of Titanium Dioxide Thin Films. *Chem. Mater.* **1993**, *5*, 1174−1181.
(63) Walia, S. *Low Power Semiconductor Devices and Processes for Emerging Applications in Communications, Computing, and Sensing*; CRC Press, 2018.
(64) *IEEE International Interconnect Technology Conference/Advanced Metallization Conference*; IITC/AMC, 2016; pp 133−135.
(65) Brinker, C. J. Hydrolysis and Condensation of Silicates: Effects on Structure. *J. Non-Cryst. Solids* **1988**, *100*, 31−50.
(66) Lebrun, J. J.; Porte, H. Polysiloxanes. *Compr. Polym. Sci.* **1989**, *5*, 593−609.
(67) Siefering, K. L.; Griffin, G. L. Growth Kinetics of CVD TiO2: Influence of Carrier Gas. *J. Electrochem. Soc.* **1990**, *137*, 1206−1208.
(68) Barr, T. L.; Seal, S. Nature of the Use of Adventitious Carbon as a Binding Energy Standard. *J. Vac. Sci. Technol., A* **1995**, *13*, 1239−1246.
(69) Ma, K.-X.; Ho, C.-H.; Zhu, F.; Chung, T.-S. Investigation of Surface Energy for Organic Light Emitting Polymers and Indium Tin Oxide. *Thin Solid Films* **2000**, *371*, 140−147.
(70) Rodgers, M. T.; Stanley, J. R.; Amunugama, R. Periodic Trends in the Binding of Metal Ions to Pyridine Studied by Threshold Collision-Induced Dissociation and Density Functional Theory. *J. Am. Chem. Soc.* **2000**, *122*, 10969−10978.
(71) Kennemur, J. G. Poly(Vinylpyridine) Segments in Block Copolymers: Synthesis, Self-Assembly, and Versatility. *Macromolecules* **2019**, *52*, 1354−1370.
(72) Giraud, E. C.; Mokarian-Tabari, P.; Toolan, D. T. W.; Arnold, T.; Smith, A. J.; Howse, J. R.; Topham, P. D.; Morris, M. A. Highly Ordered Titanium Dioxide Nanostructures via a Simple One-Step Vapor-Inclusion Method in Block Copolymer Films. *ACS Appl. Nano Mater.* **2018**, *1*, 3426−3434.
(73) Sierański, T. Discovering the Stacking Landscape of a Pyridine-Pyridine System. *J. Mol. Model.* **2017**, *23*, 338.
(74) Brittain, W. J.; Minko, S. A Structural Definition of Polymer Brushes. *J. Polym. Sci., Part A: Polym. Chem.* **2007**, *45*, 3505−3512.
(75) Cassie, A. B. D.; Baxter, S. Wettability of Porous Surfaces. *Trans. Faraday Soc.* **1944**, *40*, 546−551.
(76) Lundy, R.; Byrne, C.; Bogan, J.; Nolan, K.; Collins, M. N.; Dalton, E.; Enright, R. Exploring the Role of Adsorption and Surface State on the Hydrophobicity of Rare Earth Oxides. *ACS Appl. Mater. Interfaces* **2017**, *9*, 13751.
(77) Laibinis, P. E.; Whitesides, G. M. Omega.-Terminated Alkanethiolate Monolayers on Surfaces of Copper, Silver, and Gold Have Similar Wettabilities. *J. Am. Chem. Soc.* **1992**, *114*, 1990−1995.
(78) Wenzel, R. N. Resistance of Solid Surfaces to Wetting by Water. *Ind. Eng. Chem.* **1936**, *28*, 988−994.
(79) Jouault, N.; Dalmas, F.; Said, S.; Di Cola, E.; Schweins, R.; Jestin, J.; Boué, F. Direct Measurement of Polymer Chain Conformation in Well-Controlled Model Nanocomposites by Combining SANS and SAXS. *Macromolecules* **2010**, *43*, 9881−9891.
(80) Liu, F.-M.; Wang, T.-M. Surface and Optical Properties of Nanocrystalline Anatase Titania Films Grown by Radio Frequency Reactive Magnetron Sputtering. *Appl. Surf. Sci.* **2002**, *195*, 284−290.
(81) Post, P.; Wurlitzer, L.; Maus-Friedrichs, W.; Weber, A. Characterization and Applications of Nanoparticles Modified In-Flight with Silica or Silica-Organic Coatings. *Nanomaterials* **2018**, *8*, 530.
(82) Hannula, M.; Ali-Löytty, H.; Lahtonen, K.; Sarlin, E.; Saari, J.; Valden, M. Improved Stability of Atomic Layer Deposited Amorphous TiO_2 Photoelectrode Coatings by Thermally Induced Oxygen Defects. *Chem. Mater.* **2018**, *30*, 1199−1208.
(83) Snelgrove, M.; Zehe, C.; Lundy, R.; Yadav, P.; Rueff, J.-P.; O'Connor, R.; Bogan, J.; Hughes, G.; McGlynn, E.; Morris, M.; et al. Surface Characterization of Poly-2-Vinylpyridine—A Polymer for Area Selective Deposition Techniques. *J. Vac. Sci. Technol., A* **2019**, *37*, 050601.
(84) Si, W.; Lei, W.; Hao, Q.; Xia, X.; Zhang, H.; Li, J.; Li, Q.; Cong, R. Facile Synthesis of Nitrogen-Doped Graphene Derived from Graphene Oxide and Vitamin B3 as High-Performance Sensor for Imidacloprid Determination. *Electrochim. Acta* **2016**, *212*, 784−790.
(85) Ganesh, V. A.; Raut, H. K.; Nair, A. S.; Ramakrishna, S. A Review on Self-Cleaning Coatings. *J. Mater. Chem.* **2011**, *21*, 16304−16322.
(86) Usai, S.; Walsh, J. J. Facile Assembly of Polyoxometalate-Polyelectrolyte Films on Nano-MO2(M=Sn, Ti) for Optical Applications. *J. Electroanal. Chem.* **2018**, *815*, 86−89.
(87) Busani, T.; Devine, R. A. B. Dielectric and Infrared Properties of TiO_2 Films Containing Anatase and Rutile. *Semicond. Sci. Technol.* **2005**, *20*, 870−875.
(88) Rahimi, N.; Pax, R. A.; Gray, E. M. Review of Functional Titanium Oxides. I: TiO2and Its Modifications. *Prog. Solid State Chem.* **2016**, *44*, 86−105.
(89) Daubert, J. S.; Hill, G. T.; Gotsch, H. N.; Gremaud, A. P.; Ovental, J. S.; Williams, P. S.; Oldham, C. J.; Parsons, G. N. Corrosion Protection of Copper Using Al_2O_3, TiO_2, ZnO, HfO_2, and ZrO_2 Atomic Layer Deposition. *ACS Appl. Mater. Interfaces* **2017**, *9*, 4192−4201.
(90) Zardetto, V.; Williams, B. L.; Perrotta, A.; Di Giacomo, F.; Verheijen, M. A.; Andriessen, R.; Kessels, W. M. M.; Creatore, M. Atomic Layer Deposition for Perovskite Solar Cells: Research Status, Opportunities and Challenges. *Sustainable Energy and Fuels*; Royal Society of Chemistry, 2017; pp 30−55.
(91) Liao, S.-Y.; Yang, Y. C.; Huang, S. H.; Gan, J. Y. Synthesis of Pt@TiO2@CNTs Hierarchical Structure Catalyst by Atomic Layer Deposition and Their Photocatalytic and Photoelectrochemical Activity. *Nanomaterials* **2017**, *7*, 97.
(92) Kulmas, M.; Paterson, L.; Höflich, K.; Bashouti, M. Y.; Wu, Y.; Göbelt, M.; Ristein, J.; Bachmann, J.; Meyer, B.; Christiansen, S. Composite Nanostructures of TiO_2 and ZnO for Water Splitting Application: Atomic Layer Deposition Growth and Density Functional Theory Investigation. *Adv. Funct. Mater.* **2016**, *26*, 4882−4889.

https://dx.doi.org/10.1021/acs.langmuir.0c02512
Langmuir 2020, 36, 12394−12402